Materials Advances

ROYAL SOCIETY OF CHEMISTRY

COMMUNICATION

View Article Online
View Journal | View Issue

Cite this: *Mater. Adv.*, 2025, 6, 963

Received 25th November 2024,
Accepted 17th January 2025

DOI: 10.1039/d4ma01114g

rsc.li/materials-advances

Nano- and ultra-dispersed ZnO and $ZnFe_2O_4$ on graphitic carbon nitride as photoelectrocatalysts for the ethanol oxidation reaction†

Tommaso Sturaro,[a] Mattia Benedet,[ab] Mattia Brugia,[a] Giacomo Marchiori,[a] Gian Andrea Rizzi,[ab] Alberto Gasparotto,[ab] Davide Barreca,*[b] Oleg I. Lebedev[c] and Chiara Maccato[ab]

The sustainable production of hydrogen fuel through biomass-derived ethanol valorization is directly dependent on the availability of eco-friendly and efficient electrocatalysts for possible real-world end-uses. To this aim, graphitic carbon nitride (gCN) supported on flexible carbon cloths *via* electrophoretic deposition was functionalized with nano- and ultra-dispersed ZnO and $ZnFe_2O_4$ co-catalysts by cold plasma sputtering. The developed materials were tested for the first time as electrocatalysts for the ethanol oxidation reaction (EOR) in alkaline media, paving the way to the implementation of promising and inexpensive noble metal-free systems for green energy generation.

The significant overreliance on the fossil fuel reservoir has boosted increasing attention on sustainable energy generation, compliant with the ever more stringent environmental regulations.[1,2] Accordingly, several efforts worldwide are dedicated to developing solutions aimed at satisfying the global energy demand in a greener perspective.[3] Among the viable processes, the ethanol oxidation reaction (EOR) holds remarkable promise, thanks to the ethanol (EtOH) high energy density (8.0 kW h kg^{-1}) and low toxicity.[4] Besides being of importance for use in direct ethanol fuel cells (DEFCs),[5] EOR can be coupled with the hydrogen evolution reaction (HER) to upgrade biomass-derived ethanol, increasing the return of energy investment in comparison to the more investigated water splitting processes.[6] However, eco-friendly and highly active electrocatalysts, as an alternative to the widely-used Pt/C ones, are strictly necessary in order to implement such processes for eventual real-world applications.

In this context, graphitic carbon nitride (gCN) has become a rising star over the last few years, thanks to its non-toxicity, low cost, excellent stability, tuneable electronic structure, and Vis-light response ($E_G \approx 2.7$ eV).[6–13] Nevertheless, its intrinsic activity is limited by the low specific surface area and fast recombination rate of photogenerated electrons and holes.[14] These drawbacks can be bypassed through controlled functionalization with suitable co-catalysts[15] containing metal centres, whose introduction in gCN can yield multi-component systems featuring improved properties.[6] Among the possible candidates, ZnO, a wide band gap semiconductor ($E_G \approx 3.4$ eV),[16] possesses various appealing characteristics, such as high stability, environmental friendliness, and good electron mobility.[17] Furthermore, zinc ferrite ($ZnFe_2O_4$), a magnetic spinel-type system with a narrower band gap ($E_G \approx 1.9$ eV),[18] offers a good stability and excellent redox properties,[19] rendering it a valuable oxidation co-catalyst thanks also to the presence of Fe(III) centres, serving as additional active sites. Nonetheless, such advantages are partially eclipsed by the high electron–hole recombination, overshadowing the resulting functional performances.[20]

Based on the above observations, the combination of gCN with ZnO or $ZnFe_2O_4$ represents an amenable toolkit to fabricate EOR (photo)electrocatalysts featuring improved functional performances. The latter can be successfully achieved through a modular construction of nano-heterojunctions accelerating the reaction kinetics,[20] and suppressing detrimental charge carrier recombination processes.[7] Nonetheless, to the best of our knowledge, no literature reports on supported gCN–ZnO and gCN–$ZnFe_2O_4$ electrocatalysts for the ethanol oxidation reaction in alkaline media are available to date.

In the present study, we propose new photoelectrocatalysts based on gCN architectures functionalized with nano- and ultra-dispersed ZnO and $ZnFe_2O_4$ for the EOR in alkaline media. Material fabrication was performed using an original multi-step preparation strategy, involving the electrophoretic deposition (EPD) of gCN on high area, flexible carbon cloth supports, followed by functionalization with ZnO and $ZnFe_2O_4$

[a] *Department of Chemical Sciences, Padova University and INSTM, 35131, Padova, Italy*
[b] *CNR-ICMATE and INSTM, Department of Chemical Sciences, Padova University, 35131, Padova, Italy. E-mail: davide.barreca@unipd.it*
[c] *Laboratoire CRISMAT, UMR 6508 Normandie Université, CNRS, ENSICAEN, UNICAEN, 14050, Caen, Cedex 4, France*

† Electronic supplementary information (ESI) available: Details on material synthesis, characterization and functional tests. See DOI: https://doi.org/10.1039/d4ma01114g

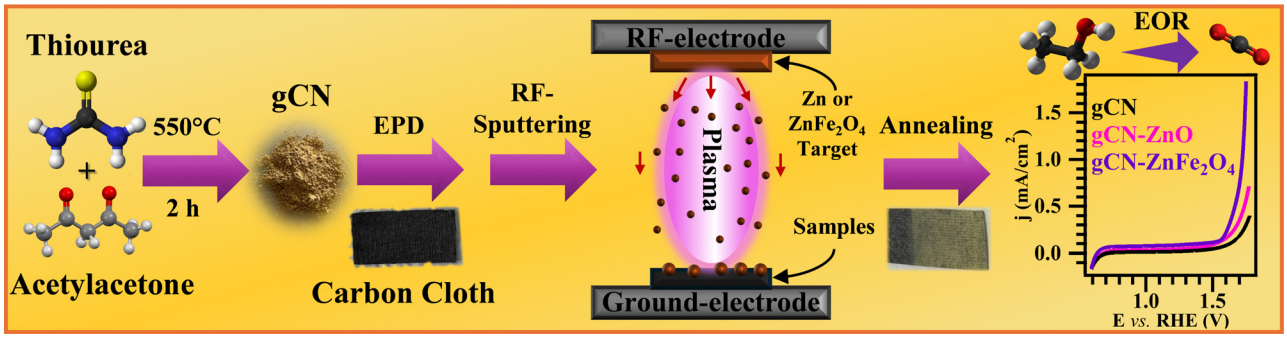

Scheme 1 Sketch of the multi-step route used for the preparation of gCN-based electrocatalysts. The photographs of the pristine carbon cloth and of a representative sample are also displayed.

via radio frequency (RF)-sputtering from non-equilibrium plasmas (Scheme 1). A multi-technique characterization using complementary techniques was carried out with particular focus on the interplay between gCN and the introduced co-catalysts, investigating its influence on the ultimate photoinduced EOR performances. As discussed below, the target systems yield an amenable activity increase in comparison to the pristine gCN, along with a favourable operational stability.

Preliminary FT-IR analyses (see Fig. S1a and pertaining comments, ESI†) evidenced the characteristic vibrational modes of graphitic carbon nitride containing an appreciable content of uncondensed amino groups. The band gap values estimated from optical measurements (Fig. S1b and c, ESI;† $E_G \approx 2.3$–2.4 eV) were lower in comparison to literature data,[6,7] suggesting an enhanced Vis-light harvesting for the target specimens. Photoluminescence (PL) spectra (Fig. S1d, ESI† and related observations) indicated that the strong emission signal observed for bare gCN, originating from the recombination of photogenerated electrons and holes in graphitic carbon nitride, underwent a marked decrease upon functionalization with ZnO, and, even more, with $ZnFe_2O_4$. This phenomenon evidenced the occurrence of an efficient charge transfer between the system components, particularly in the case of zinc ferrite, indicating that the recombination of photogenerated electrons and holes was favourably suppressed.

X-ray photoelectron spectroscopy (XPS) provided important information on the system chemical composition. The analyses (see also Fig. S2, ESI†) revealed the presence of C, N and O signals for all specimens, along with Zn and Fe ones for functionalized samples. The C 1s photopeak (Fig. 1a and Fig. S3a, c, S4a, ESI†) was deconvoluted by five contributing bands: C_0 [binding energy (BE) = 284.8 eV], due to both adventitious carbon and C–C bonds from the carbon cloth substrate;[8,21] C_1 (286.3 eV), arising mainly from C–NH_x species ($x = 1, 2$) on gCN edges,[22] but also from C–O–C and C–OH groups arising from atmospheric exposure;[23] C_2 (288.8 eV), attributed to C in N–C=N moieties within gCN;[24,25] C_3 (289.6 eV), related to carboxylic and ester groups of the carbon cloth;[26] C_4 (294.4 eV), due to π-electron excitation.[27] Four components contributed to the N 1s peak (Fig. 1b and Fig. S3b and d; see also Fig. S4a, ESI†): N_0 (398.7 eV) and N_1 (399.8 eV) corresponded to bi-coordinated (C–N=C, N_{2c})[28] and tri-coordinated

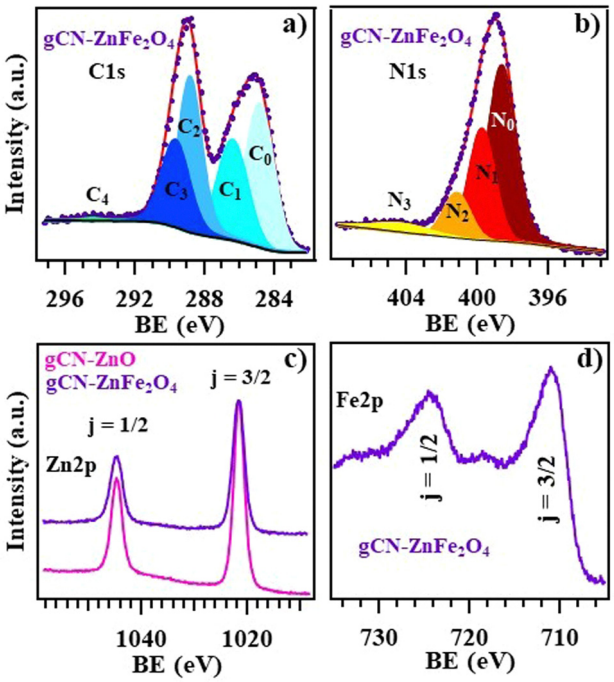

Fig. 1 (a) C 1s and (b) N 1s photopeaks for gCN–$ZnFe_2O_4$. (c) Zn 2p and (d) Fe 2p photopeaks for gCN–ZnO and gCN–$ZnFe_2O_4$ specimens.

[N–$(C)_3$] nitrogen atoms in gCN,[11] respectively; N_2 (401.2 eV), assigned to amino groups;[11,29] N_3 (404.3 eV), ascribed to π-electron excitation.[8] As displayed in Fig. S4b (ESI†), the contribution of component N_2 to the N 1s peak increased according to the following trend: gCN < gCN–ZnO < gCN–$ZnFe_2O_4$. This result suggested a parallel enhancement of the –NH_x group content in the resulting materials, due to plasma bombardment during RF-sputtering experiments, whose duration was appreciably higher for $ZnFe_2O_4$ functionalization in comparison to the ZnO one (see the ESI,† § S1–S2). Details regarding O 1s peak fitting are reported in the ESI† (§ S2, Fig. S5 and related comments, ESI†). In gCN–ZnO and gCN–$ZnFe_2O_4$ specimens, Zn $2p_{3/2}$ peaks (Fig. 1c) were located at BE = 1021.9 and 1021.8 eV, and the corresponding Auger parameters were estimated to be 2010.3 eV and 2011.0 eV [see the ZnLMM Auger signals in Fig. S6, and eqn (S1) in the ESI†].

These results confirmed the successful functionalization of carbon nitride with ZnO[30,31] and $ZnFe_2O_4$,[25,32] respectively. Finally, the Fe $2p_{3/2}$ signal shape and position [Fig. 1d; BE(Fe $2p_{3/2}$) = 711.0 eV, spin–orbit splitting = 13.1 eV] were consistent with previous literature data for $ZnFe_2O_4$.[7,32]

Scanning electron microscopy (SEM) images displayed gCN aggregates, characterized by a highly porous sheet-like morphology, homogenously distributed over the underlying carbon cloth fibres (Fig. S7, ESI†), whereas X-ray diffraction (XRD, Fig. S8, ESI†) analyses showed only signals related to the substrate. To attain a deeper insight into the system nano-organization and spatial distribution of ZnO and $ZnFe_2O_4$, transmission electron microscopy (TEM) and related analyses were undertaken. The results obtained for gCN–ZnO (Fig. 2a and b; see also Fig. S9a and b, ESI†) evidenced the open and sheet-like morphology of gCN flakes. Elemental mapping (Fig. 2c) confirmed the presence of Zn and O, besides C and N. The former elements were characterized by a highly spread distribution, which was related to the presence of low-sized ZnO nanocrystals (Fig. 2d and e). As regards gCN–$ZnFe_2O_4$ (Fig. 2f–h; see also Fig. S9c and d, ESI†), no diffraction rings attributable to $ZnFe_2O_4$ were detected, and no zinc ferrite nanoparticles could be distinctly observed. Nonetheless, a careful inspection of the image reported in Fig. 2g highlighted the occurrence of bright contrast dots, indicating the presence of ultra-dispersed $ZnFe_2O_4$, in line with the EDXS and XPS results (see above). An analogous "quasi-atomic" dispersion of nickel(II) oxide was recently reported by us in gCN–NiO photoelectrocatalysts for the oxygen evolution reaction, fabricated *via* a liquid phase route.[8]

The higher dispersion of $ZnFe_2O_4$ with respect to ZnO could be traced back to the higher amino group content for gCN–$ZnFe_2O_4$ in comparison to gCN–ZnO (see above). In fact, these groups can act as grafting sites favoring co-catalyst anchoring to gCN and yielding, at the same time, an enhanced co-catalyst dispersion. As a result, charge transfer phenomena between the system components can be deemed to be enhanced.[8,33] Overall, TEM results demonstrate an intimate contact between gCN and oxide co-catalysts, in particular for $ZnFe_2O_4$, a favorable issue to benefit from their mutual interplay and achieve improved performances (see below).

The EOR activity of the target systems was investigated in alkaline media. Fig. 3a displays linear scanning voltammetry (LSV) curves recorded under illumination. As can be observed, gCN–ZnO and gCN–$ZnFe_2O_4$ specimens exhibited improved EOR performances with respect to the pristine gCN, according to the following trend: gCN–$ZnFe_2O_4$ > gCN–ZnO > gCN. This trend was maintained even in the absence of ethanol in the reaction medium (Fig. S10a, ESI†) and under dark conditions (Fig. S10b, ESI†). A comparison of the curves plotted in Fig. 3a and Fig. S10 (ESI†) evidenced an appreciable increase of the recorded *j* values upon ethanol addition, confirming thus a direct EOR contribution to the overall current density, and highlighting also the photoactive behaviour of the target electrocatalysts. In addition, a favourable shift of the onset potential to lower values for gCN–ZnO and gCN–$ZnFe_2O_4$ was observed (Table S1, ESI†). Overall, these results underscored gCN–$ZnFe_2O_4$ as the best photoelectrocatalyst in the whole family, as also

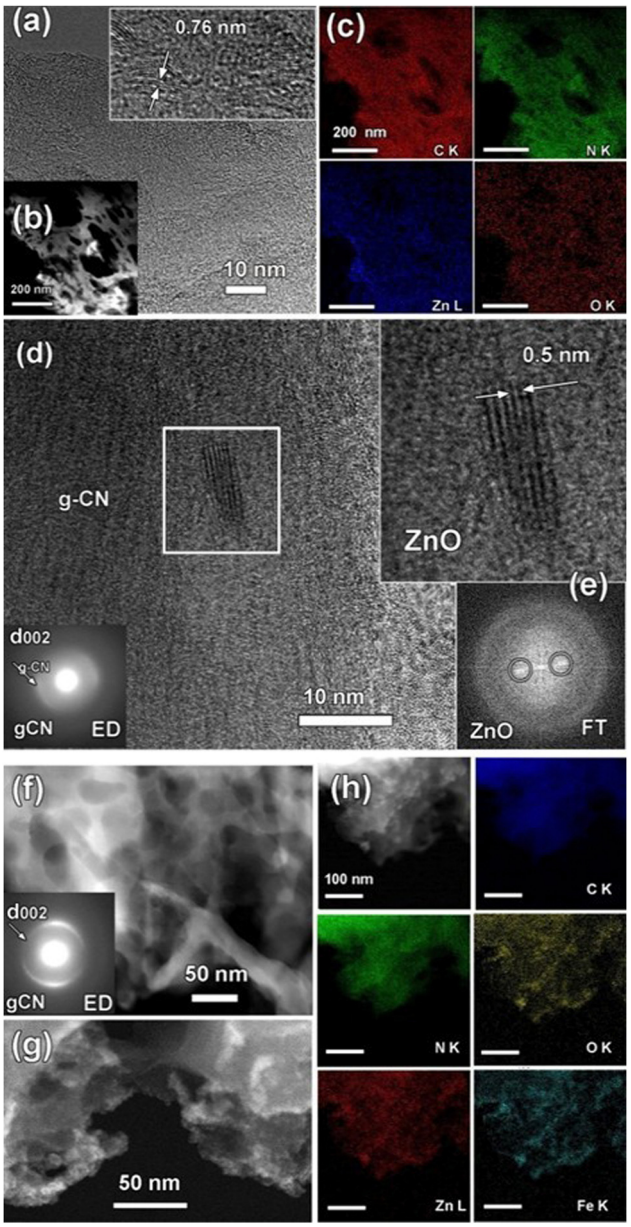

Fig. 2 (a) Bright field-high resolution TEM (BF-HRTEM) image of gCN–ZnO. Inset: Magnified HRTEM image marking the distance between (001) gCN lattice planes. (b) Low magnification high angle annular dark field-scanning TEM (HAADF-STEM) image and (c) simultaneously acquired energy dispersive X-ray spectroscopy (EDXS)-STEM elemental maps. (d) BF-HRTEM image of gCN–ZnO, and corresponding electron diffraction (ED) pattern. (e) HRTEM image and Fourier transform (FT) pattern, confirming the occurrence of crystalline ZnO, for the nanoparticle framed in (d). The (001) ZnO lattice planes are marked. (f) HAADF-STEM image of gCN–$ZnFe_2O_4$ and corresponding ED pattern. (g) HAADF-STEM image for the same specimen, showing ultra-dispersed $ZnFe_2O_4$. (h) Low magnification HAADF-STEM image and simultaneously acquired EDXS-STEM elemental maps for gCN–$ZnFe_2O_4$.

testified by the applied bias photon-to-current efficiency (ABPE) curves [Fig. 3b; see also the ESI,† eqn (S3)]. This conclusion was also validated by the analysis of the Tafel slope values (Fig. 3c and Fig. S11, ESI†), that yielded the following trend: gCN > gCN–ZnO > gCN–$ZnFe_2O_4$, indicating a more favourable reaction kinetics for the

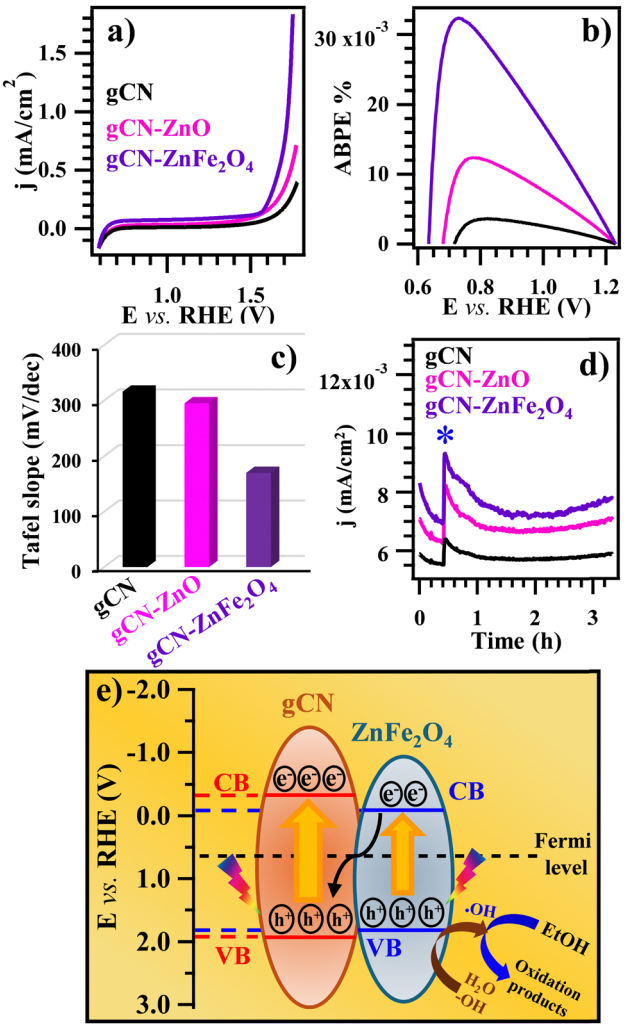

Fig. 3 (a) LSV curves obtained in KOH 0.5 M + EtOH 0.5 M under irradiation. (b) ABPE (%) curves. (c) Tafel slope values under irradiation, corresponding to LSV curves in panel (a). (d) CA data for gCN, gCN–ZnO and gCN–$ZnFe_2O_4$ at 1.55 V *vs.* RHE under illumination. EtOH introduction in the working solution is marked by *. (e) Sketch of the interfacial band structure for the gCN/$ZnFe_2O_4$ heterojunction.

functionalized electrocatalysts, and especially for gCN–$ZnFe_2O_4$. Additional information was provided by chronoamperometry (CA) measurements performed in bare KOH solutions for the first 30 minutes and, subsequently, in KOH + EtOH aqueous solutions (Fig. 3d). Immediately after EtOH introduction, current density underwent an increase to a maximum value and a subsequent reduction, indicating the occurrence of ethanol consumption at the electrode surface and an appreciable catalytic activity.[34]

Table S1 (ESI†) summarizes the most relevant electrochemical data for the target electrocatalysts. Remarkably, current density values and Tafel slopes for the present functionalized specimens compare favourably with those reported so far for various electrocatalysts for alcohol oxidation based on functionalized gCN or carbonaceous materials, and even for different widely used platinum–carbon ones (Table S2, ESI†).

In view of eventual real-world end-uses of the developed systems for energy conversion and storage, the photoelectrocatalyst stability is a primary issue.[7] As concerns materials based on graphitic carbon nitride, the stability upon prolonged operation is, in general, influenced by the synthesis route and by gCN combination with other partners to yield composite systems.[35] In the present work, the target materials were stored for six months under ordinary laboratory conditions, and periodically subjected to electrochemical tests (Fig. S12, ESI†). The latter evidenced the occurrence of very limited photocurrent density variations, underscoring thus an attractive operational stability, an important figure of merit. This conclusion was further corroborated by *post operando* XPS analyses (Fig. S13 and S14, ESI†), that enabled us to discard any significant material alteration/degradation upon prolonged testing. Altogether, these results evidence the applicative potential of the present systems towards the implementation of environmentally friendly and cost-effective EOR photoelectrocatalysts for practical applications.

In order to better elucidate the EOR performance enhancement afforded by carbon nitride functionalization, the interfacial electronic interplay between the hosting gCN and the functionalizing metal oxides (ZnO and $ZnFe_2O_4$) was examined. The Fermi level (E_F) energy positions can be approximated to the flat band potential, which, in turn, can be estimated by the intercept of the square photocurrent density curves with the potential axis[36] (Fig. S15a, ESI†). Thanks to the difference between E_F and valence band (VB) edges (see Fig. S15b, ESI†), it was possible to set the VB edge position for gCN, ZnO, and $ZnFe_2O_4$. Subsequently, the optical band gap values of gCN (see above), ZnO (3.37 eV)[16] and $ZnFe_2O_4$ (1.90 eV)[18] allowed us to derive the corresponding conduction band (CB) positions. The obtained values were used to build up the diagrams proposed in Fig. 3e and Fig. S16 (ESI†). For both gCN–ZnO and gCN–$ZnFe_2O_4$, a Z-type junction scheme accounts for the improved EOR functional performances in comparison to the pristine carbon nitride. The experimental proof of the existence of this Z-scheme junction is provided by the increase in the photocurrent density and ABPE values observed upon gCN functionalization[7] (see above and Fig. 3a and b). According to this configuration, photogenerated electrons reach the counter-electrode through gCN (the main system component in contact with the carbon cloth substrate), whereas photoproduced holes remain localized on ZnO or $ZnFe_2O_4$ VB and promote the ethanol oxidation process. The present electrochemical tests revealed a better photoactivity for gCN–$ZnFe_2O_4$, which can be explained based on the synergistic concurrence of different phenomena. Besides the narrower $ZnFe_2O_4$ band gap in comparison to ZnO, a key factor is the ultra-dispersion of $ZnFe_2O_4$ in the hosting gCN, promoted by the highest amino group content in the present electrocatalyst family (see above), which enhances the contact area between the system components in comparison to the case of gCN–ZnO. As a consequence, the improved gCN/co-catalyst interaction due to the higher density of heterojunctions promotes, in turn, a better activity thanks to the enhanced separation of photogenerated electrons and holes.[8] The latter effect is further amplified by the increased –NH_x content for gCN–$ZnFe_2O_4$ in comparison to gCN–ZnO (see above and Fig. S4b, ESI†), since the related defects may act as capturing sites, favorably affecting the ultimate functional performances.[7,28]

In summary, this work was focused on the preparation and characterization of gCN–ZnO and gCN–$ZnFe_2O_4$ electrocatalysts for ethanol oxidation in alkaline media. These systems, never proposed to date for such end-uses, were fabricated using an original synthetic route, involving: (i) the electrophoretic deposition of graphitic carbon nitride on flexible carbon cloth substrates; (ii) functionalization with ZnO or $ZnFe_2O_4$ *via* sputtering under mild operational conditions. The modular formation of heterojunctions between the system components, benefitting from their intimate contact, especially in the case of ultra-dispersed $ZnFe_2O_4$, yielded an attractive catalytic activity towards the EOR in alkaline media. This result, accompanied by the good material stability, could trigger the development of eco-friendly and cost-effective catalytic platforms contributing to the broader goal of sustainable energy solutions for real-world applications.

Data availability

All the data supporting this article have been included as part of the ESI.†

Conflicts of interest

There are no conflicts to declare.

Acknowledgements

The authors gratefully acknowledge financial support received from CNR (Progetti di Ricerca @CNR – avviso 2020 – ASSIST), Padova University (P-DiSC#02BIRD2023-UNIPD RIGENERA, DOR 2022–2024), European Union (SCI-TROPHY project, call MUR PRIN 2022, Prot. 2022474YE8) and INSTM Consortium (TRI.25/013 – CIMENTO).

Notes and references

1 W. Li, H. Tian, L. Ma, Y. Wang, X. Liu and X. Gao, *Mater. Adv.*, 2022, **3**, 5598–5644.
2 A. Jamma, B. Jaksani, C. S. Vennapoosa, S. Gonuguntla, S. Sk, M. Ahmadipour, M. Abraham B, I. Mondal and U. Pal, *Mater. Adv.*, 2024, **5**, 2785–2796.
3 K. Bramhaiah and S. Bhattacharyya, *Mater. Adv.*, 2022, **3**, 142–172.
4 L. Yaqoob, T. Noor and N. Iqbal, *RSC Adv.*, 2021, **11**, 16768–16804.
5 Z. Hu, N. Yang, Y. Feng, L. Xu, C. Hu, H. Liu, S. Tian and J. Yang, *Chem. Commun.*, 2023, **59**, 4020–4023.
6 M. Brugia, M. Benedet, G. A. Rizzi, A. Gasparotto, D. Barreca, O. I. Lebedev and C. Maccato, *ChemSusChem*, 2024, **17**, e202401041.
7 M. Benedet, G. A. Rizzi, A. Gasparotto, N. Gauquelin, A. Orekhov, J. Verbeeck, C. Maccato and D. Barreca, *Appl. Surf. Sci.*, 2023, **618**, 156652.
8 E. Scattolin, M. Benedet, G. A. Rizzi, A. Gasparotto, O. I. Lebedev, D. Barreca and C. Maccato, *ChemSusChem*, 2024, **17**, e202400948.
9 P. O. Ohemeng and R. Godin, *Chem. Commun.*, 2024, **60**, 12034–12061.
10 I. J. Budiarso, V. A. Dabur, R. Rachmantyo, H. Judawisastra, C. Hu and A. Wibowo, *Mater. Adv.*, 2024, **5**, 2668–2688.
11 H. Moussa, B. Chouchene, T. Gries, L. Balan, K. Mozet, G. Medjahdi and R. Schneider, *ChemCatChem*, 2018, **10**, 4973–4983.
12 X. Zou, Z. Sun and Y. H. Hu, *J. Mater. Chem. A*, 2020, **8**, 21474–21502.
13 T. S. Miller, A. B. Jorge, T. M. Suter, A. Sella, F. Corà and P. F. McMillan, *Phys. Chem. Chem. Phys.*, 2017, **19**, 15613–15638.
14 M. Z. Rahman and C. B. Mullins, *Acc. Chem. Res.*, 2019, **52**, 248–257.
15 N. Rono, J. K. Kibet, B. S. Martincigh and V. O. Nyamori, *Crit. Rev. Solid State Mater. Sci.*, 2020, **46**, 189–217.
16 S. S. Kumar, P. Venkateswarlu, V. R. Rao and G. N. Rao, *Int. Nano Lett.*, 2013, **3**, 30.
17 I. L. Ouriques Brasileiro, V. S. Madeira, A. L. Lopes-Moriyama and M. L. Rodrigues de Almeida Ramalho, *Ceram. Int.*, 2023, **49**, 4449–4459.
18 K. Wu, J. Li and C. Zhang, *Ceram. Int.*, 2019, **45**, 11143–11157.
19 C. Cai, Z. Zhang, J. Liu, N. Shan, H. Zhang and D. D. Dionysiou, *Appl. Catal., B*, 2016, **182**, 456–468.
20 J. Han, Y. Lan, Q. Song, H. Yan, J. Kang, Y. Guo and Z. Liu, *Chem. Commun.*, 2020, **56**, 13205–13208.
21 Y. Yang, G. Zeng, D. Huang, C. Zhang, D. He, C. Zhou, W. Wang, W. Xiong, X. Li, B. Li, W. Dong and Y. Zhou, *Appl. Catal., B*, 2020, **272**, 118970.
22 C.-Q. Xu, W.-D. Zhang, K. Deguchi, S. Ohki, T. Shimizu, R. Ma and T. Sasaki, *J. Mater. Chem. A*, 2020, **8**, 13299–13310.
23 I. Bertóti, M. Mohai and K. László, *Carbon*, 2015, **84**, 185–196.
24 H. Wang, Y. Fu, X. Liu, R. Yang, Y. Hu, D. Liu, J. Wan and Z. Zeng, *Sens. Actuators, B*, 2023, **377**, 132796.
25 S. Borthakur and L. Saikia, *J. Environ. Chem. Eng.*, 2019, **7**, 103035.
26 O. Pérez, O. F. Odio and E. Reguera, *New J. Chem.*, 2022, **46**, 11255–11265.
27 M. I. Nabeel, D. Hussain, N. Ahmad, H.-M. Xiao and S. G. Musharraf, *Environ. Sci.: Nano*, 2023, **10**, 2810–2830.
28 M. Benedet, A. Gallo, C. Maccato, G. A. Rizzi, D. Barreca, O. I. Lebedev, E. Modin, R. McGlynn, D. Mariotti and A. Gasparotto, *ACS Appl. Mater. Interfaces*, 2023, **15**, 47368–47380.
29 J. Ding, X. Sun, Q. Wang, D.-S. Li, X. Li, X. Li, L. Chen, X. Zhang, X. Tian and K. Ostrikov, *J. Alloys Compd.*, 2021, **873**, 159871.
30 L. Dake, D. Baer and J. Zachara, *Surf. Interface Anal.*, 1989, **14**, 71–75.
31 D. Barreca, A. Gasparotto, C. Maccato, C. Maragno and E. Tondello, *Surf. Sci. Spectra*, 2007, **14**, 19–26.
32 D. Peeters, D. H. Taffa, M. M. Kerrigan, A. Ney, N. Jöns, D. Rogalla, S. Cwik, H.-W. Becker, M. Grafen and A. Ostendorf, *ACS Sustainable Chem. Eng.*, 2017, **5**, 2917–2926.

33 M. Benedet, G. A. Rizzi, O. I. Lebedev, V. Roddatis, C. Sada, J.-L. Wree, A. Devi, C. Maccato, A. Gasparotto and D. Barreca, *J. Mater. Chem. A*, 2023, **11**, 21595–21609.
34 L. Bigiani, T. Andreu, C. Maccato, E. Fois, A. Gasparotto, C. Sada, G. Tabacchi, D. Krishnan, J. Verbeeck, J. R. Morante and D. Barreca, *J. Mater. Chem. A*, 2020, **8**, 16902–16907.
35 J. Safaei, N. A. Mohamed, M. F. Mohamad Noh, M. F. Soh, N. A. Ludin, M. A. Ibrahim, W. N. Roslam Wan Isahak and M. A. Mat Teridi, *J. Mater. Chem. A*, 2018, **6**, 22346–22380.
36 J. C. Alexander, *Surface Modifications and Growth of Titanium Dioxide for Photo-Electrochemical Water Splitting*, Springer Theses, 2016.